

This is the accepted manuscript made available via CHORUS. The article has been published as:

# Entropy- and purity-tailored broadband entanglement from vectorial four-wave mixing: Insights from pulse modes and classical-field dynamics

N. L. Petrov, A. A. Voronin, A. B. Fedotov, and A. M. Zheltikov

Phys. Rev. A **100**, 033837 — Published 30 September 2019

DOI: [10.1103/PhysRevA.100.033837](https://doi.org/10.1103/PhysRevA.100.033837)

# **Entropy- and purity-tailored broadband entanglement from vectorial four-wave mixing: Insights from pulse modes and classical-field dynamics**

**N. L. Petrov,<sup>1</sup> A. A. Voronin,<sup>1,3,4</sup> A. B. Fedotov,<sup>1,3,4</sup> and A. M. Zheltikov<sup>1,2,3,4</sup>**

<sup>1</sup>Physics Department, International Laser Center, M.V. Lomonosov Moscow State University, Moscow 119992, Russia

<sup>2</sup>Department of Physics and Astronomy, Texas A&M University, College Station, Texas 77843, USA

<sup>3</sup>Russian Quantum Center, Skolkovo, Moscow Region 143025, Russia

<sup>4</sup>Kazan Quantum Center, A.N. Tupolev Kazan National Research Technical University, 420126 Kazan, Russia

We present a time-domain Schmidt-mode analysis of a broadband continuous-variable entanglement of photon pairs generated via a vectorial four-wave mixing (FWM) of ultrashort laser pulses in a highly nonlinear birefringent optical fiber. We demonstrate that the time-domain eigenmodes of high-purity two-photon states generated through vectorial FWM can be steered, by varying the pump wavelength and FWM polarization geometry, from a high-purity entangled ket to a high-entropy entangled state in a space of a very high dimensionality. Moreover, this pulse-mode analysis is shown to provide a clear physical perspective on how the entanglement structure of two-photon states builds up as a result of short-pulse FWM dynamics. This insight reveals a correspondence-type relation between the quantum and classical pictures of photon-pair generation. With an eye on practical applications, a clear understanding of the temporal profile of pulse modes representing high-purity two-photon states is central to a meaningful shaping of ultrashort photon-packet waveforms for super-resolving microscopy and multiphoton spectroscopy using quantum states of light.

## **I. INTRODUCTION**

High-dimensional quantum entanglement [1 - 4] is a unique resource of quantum technologies that paves the ways for an ultrahigh-density information coding in quantum communication [5, 6], quantum computations based on novel quantum logic [7], a higher

precision in quantum phase measurements [8], enhanced immunity with respect to noise [9, 10], a higher security in quantum cryptography [11], and new tests of fundamental principles of quantum theory [2, 12, 13]. Central to the implementation of quantum information strategies based on high-dimensional entanglement is the availability of individually addressable, manageable, and measurable field modes suitable for information encoding and transmission [1, 14].

Optical fields offer an access to a vast phase space of discrete and continuous variables [15, 16], defining the spatial, temporal, spectral, polarization, and spin modes of photons, thus offering unique solutions for high-dimensional quantum entanglement [17]. While some of these variables, such as the polarization angle, are defined in a space whose dimensionality is as low as two, others provide an access to a Hilbert space with an infinite number of dimensions. Specifically, various classes of spatial modes, defined by either the orientation of the wave vector or the optical angular momentum (OAM), lend an unbounded Hilbert space for high-dimensional quantum entanglement [18 – 22]. However, an access to higher dimensions in this case is achieved at the expense of beam-profile complexity, which lowers their brightness and complicates their integration into fiber-optic communication networks. As an attractive alternative solution, spectral and temporal modes of optical fields enable continuous-variable energy – time entanglement [15, 23] which is ideally suited for efficient high-dimensional information encoding [24, 25]. Unlike entanglement in spatial modes, time- or frequency-bin entanglement is fully compatible with fiber-optic transmission. Moreover, with the aid of four-wave mixing (FWM) [26 – 32], such entanglement can be generated in waveguide modes of an optical fiber, ready for use in fiber-optic communication networks.

Here, we show that vectorial four-wave mixing (FWM) of ultrashort laser pulses in a highly birefringent, highly nonlinear optical fiber can provide a source of broadband high-dimensional continuous-variable entanglement with finely tunable entropy and purity. We will demonstrate, by means of Schmidt-mode analysis, that the broadband photon-pair output of such a vectorial FWM can be steered, by varying the pump wavelength and polarization geometry, from a high-purity, low-dimensional entangled state to a high-entropy entangled state in a space of a very high dimensionality. The time-domain Schmidt-mode analysis will be shown to provide a clear physical perspective on how the entanglement structure of such two-photon states builds up as a result of short-pulse nonlinear dynamics, revealing a fundamental, correspondence-type relation between the quantum and classical pictures of photon-pair generation.

## II. TWO-PHOTON STATES VIA VECTORIAL FOUR-WAVE MIXING: SCHMIDT-MODE ANALYSIS

We consider vectorial FWM  $\omega_{p1} + \omega_{p2} = \omega_s + \omega_i$  whereby a dyad of pump fields with central frequencies  $\omega_{p1}$  and  $\omega_{p2}$  in polarization modes  $j_1$  and  $j_2$  give rise to signal and idler fields with central frequencies  $\omega_s$  and  $\omega_i$ . With vectorial FWM in a birefringent optical fiber in mind, we assume that the mode indices  $j_1$  and  $j_2$  can take one of two values,  $j_1, j_2 = f, s$ , corresponding to the fast and slow polarization modes of a birefringent optical fiber. The signal and idler fields are then also generated in one or both of these polarization states (Figs. 1a – 1e).

The photon-pair output of such an FWM process is an entangled broadband state ket, whose description generally requires a multidimensional Hilbert space. In a standard perturbative treatment [28], this two-photon state is given by

$$|\Psi\rangle = \kappa \iint F(\omega_1, \omega_2) \hat{a}_{j_1}^\dagger(\omega_1) \hat{a}_{j_2}^\dagger(\omega_2) |0\rangle_{j_1} |0\rangle_{j_2} d\omega_1 d\omega_2 \quad (1)$$

where  $\kappa$  is the optical gain,  $F(\omega_1, \omega_2)$  is the joint spectral amplitude (JSA) function,  $\hat{a}_{j_1}^\dagger(\omega)$  and  $\hat{a}_{j_2}^\dagger(\omega)$  are the creation operators for photons with a central frequency  $\omega$  in polarization modes  $j_1$  and  $j_2$ , respectively.

In the general case, the JSA function is not factorizable as a product of functions of  $\omega_1$  and  $\omega_2$ , which makes it difficult, if possible at all, to address and manage individual information-carrying field modes. To understand the mode structure of the continuous-variable entanglement of the two-photon state  $|\Psi\rangle$ , it is instructive to resort to the Schmidt decomposition of the JSA function [15, 28],

$$F(\omega_1, \omega_2) = \sum_n \sqrt{\lambda_n} \psi_n(\omega_1) \varphi_n(\omega_2) \quad (2)$$

Here,  $\lambda_n$ ,  $\psi_n(\omega)$ , and  $\varphi_n(\omega)$  are found as the eigenvalues and eigenfunctions of the integral equations

$$\int K_1(\omega, \omega') \psi_n(\omega') d\omega' = \lambda_n \psi_n(\omega) \quad (3)$$

$$\int K_2(\omega, \omega') \varphi_n(\omega') d\omega' = \lambda_n \varphi_n(\omega) \quad (4)$$

where  $K_1(\omega, \omega') = \int F(\omega, \omega'') F^*(\omega', \omega'') d\omega''$  and  $K_2(\omega, \omega') = \int F(\omega'', \omega) F^*(\omega'', \omega') d\omega''$ .

Introducing the effective creation operators,

$$\hat{b}_n^\dagger = \int \psi_n(\omega_1) \hat{a}_{j_1}^\dagger(\omega_1) d\omega_1 \quad (5)$$

$$\hat{c}_n^\dagger = \int \varphi_n(\omega_2) \hat{a}_{j_2}^\dagger(\omega_2) d\omega_2 \quad (6)$$

we can rewrite Eq. (1) for the two-photon state  $|\Psi\rangle$  as

$$|\Psi\rangle = \sum_n \sqrt{\lambda_n} \hat{b}_n^\dagger \hat{c}_n^\dagger |0\rangle_{j1} |0\rangle_{j2} \quad (7)$$

With the  $\lambda_n$  coefficients found from Eqs. (3), (4), we can quantify the entanglement in terms of the entropy [15],  $S = -\sum_n \lambda_n \log_2 \lambda_n$ . The Schmidt parameter, defined as

$K = 1 / \sum_n \lambda_n^2$ , provides a measure for the dimensionality of the Hilbert space (or the number of biphoton modes) needed to describe the entanglement [33], with the purity of the two-photon state quantified as  $p = 1/K$ .

For  $\omega_{p1} + \omega_{p2} = \omega_s + \omega_i$  FWM driven by pump fields with spectral amplitudes  $\alpha_1(\omega)$  and  $\alpha_2(\omega)$ , the JSA function is given by [28]

$$F(\omega_s, \omega_i) = \int \alpha_1(\omega') \alpha_2(\omega_s + \omega_i - \omega') \Phi(\omega', \omega_s, \omega_i) d\omega' \quad (8)$$

where

$$\Phi(\omega', \omega_s, \omega_i) = \text{sinc}\left[\Delta\beta(\omega', \omega_s, \omega_i) \frac{L}{2}\right] \exp\left[i\Delta\beta(\omega', \omega_s, \omega_i) \frac{L}{2}\right] \quad (9)$$

is the phase-matching function,  $L$  is the length of the nonlinear medium and

$$\Delta\beta(\omega', \omega_s, \omega_i) = \beta(\omega') + \beta(\omega_s + \omega_i - \omega') - \beta(\omega_s) - \beta(\omega_i) - (\gamma_1 P_1 + \gamma_2 P_2) \quad (10)$$

is the mismatch of the frequency-dependent propagation constants  $\beta(\omega)$  of the fields involved in the FWM process,  $\gamma_1$  and  $\gamma_2$  are the relevant nonlinear coefficient and  $P_1$  and  $P_2$  are the peak powers of the pump fields.

The key properties of the JSA functions of photon pairs generated through FWM and their relation to phase and group-velocity mismatch have been thoroughly studied in the earlier work (see Ref. 28 for a comprehensive analysis and an illuminating discussion of photon-pair JSA functions). Moreover, the Schmidt coefficients  $\lambda_n$  have long been in use for a quantitative characterization of the purity of the FWM photon-pair output [15]. In this work, we extend these concepts and methods by analyzing the eigenfunctions  $\psi_n(\omega)$  and  $\varphi_n(\omega)$  and eigenvalues  $\lambda_n$  of integral equations (3) and (4) with kernels  $K_1(\omega, \omega')$  and  $K_2(\omega, \omega')$  defined through suitable convolutions of the FWM photon-pair JSA functions, as explained above. We use the eigenfunctions of Eqs. (3) and (4) to define the time-domain eigenmodes of high-purity two-photon states generated via vectorial FWM processes. As one of the central results of this analysis, we demonstrate that such eigenmodes, referred to as pulse modes, can be steered, by varying the pump wavelength and FWM polarization geometry, from a high-purity entangled ket to a high-entropy entangled state in a space of a very high dimensionality. Moreover, this pulse-mode analysis is shown to provide a clear physical perspective on how the entanglement structure of two-photon states builds up as a result of short-pulse nonlinear dynamics. This insight reveals a correspondence-type relation between

the quantum and classical pictures of photon-pair generation. With an eye on a more practical side, a clear understanding of the temporal profile of pulse modes representing high-purity two-photon states is central to a meaningful shaping of ultrashort photon-packet waveforms for multiphoton spectroscopy [34 - 36] and super-resolving microscopy [37, 38] using quantum states of light.

With these goals in mind, we numerically solve Eqs. (3) and (4) for five polarization arrangements of vectorial FWM (Figs. 1a – 1e) in a polarization-maintaining optical fiber. To this end, the kernels  $K_1(\omega, \omega')$  and  $K_2(\omega, \omega')$  were discretized and represented as  $N \times N$  matrices, with  $N$  ranging from  $\sim 10^2$  to  $\sim 10^3$ , depending on the convergence rate of the numerical solution. Calculations were performed for vectorial FWM in an optical fiber whose dispersion, nonlinearity  $\gamma$ , and birefringence  $\delta n$  were varied within the range typical of highly nonlinear photonic-crystal fibers (PCFs) [39]. Short-pulse vectorial FWM in this class of fibers can provide, as the Schmidt-mode analysis shows, a bright source of photon pairs whose entanglement structure can be tailored, by varying the pump wavelength and polarization geometry, from a high-purity biphoton entanglement to a high-entropy entanglement in a space of a very high dimensionality.

Both pump fields in our calculations are taken in the form of transform-limited pulses with a pulse width of 300 fs. These pulses share the same Gaussian spectral profile  $\alpha_1(\omega) = \alpha_2(\omega) = \alpha_0 \exp[-(\omega - \omega_p)^2 / \sigma^2]$  with a variable central frequency  $\omega_p = \omega_{p1} = \omega_{p2}$  and a bandwidth  $\sigma$ . In Figs. 1f – 1j, we present the maps of the coherence length  $l_c = \pi/(2|\Delta\beta|)$  calculated as a function of the pump, signal, and idler wavelengths  $\lambda_q = 2\pi c/\omega_q$  ( $q = p, s, i$  for the pump, signal and idler fields, respectively; the wavelengths  $\lambda_q$  should not be confused with  $\lambda_n$  – the standard notation of the Schmidt coefficients) for five different polarization geometries of this FWM process, as sketched in Figs. 1a – 1e, in an optical fiber with typical parameters of a highly nonlinear, highly birefringent PCF –  $\gamma = 100 \text{ W}^{-1} \text{ km}^{-1}$ ,  $\delta n$  ranging from  $10^{-4}$  to  $10^{-3}$ , and a group-velocity dispersion (GVD) profile as shown in Fig. 2a, with the zero-GVD wavelength at  $\lambda_z \approx 740 \text{ nm}$ . This set of parameters is provided by a generic PCF structure with a core radius of about  $1.45 \text{ }\mu\text{m}$  and a hexagonal lattice of holes in the cladding with an air-filling factor of  $\approx 0.36$ . The laser peak power is set at  $P_1 = P_2 = P = 50 \text{ W}$  and the fiber length is taken as  $L = 40 \text{ cm}$ .

### III. ENTROPY- AND PURITY-TAILORED BROADBAND TWO-PHOTON STATES

As an instructive example of fiber-based entanglement engineering, Fig. 3 presents the JSA functions and the Schmidt eigenvalues calculated for a photon-pair FWM output of a fiber with the above-specified parameters driven by two cross-polarized pump fields, giving rise to

the signal and idler fields detected in the  $s$  and  $f$  polarization modes, respectively (Fig. 1d). This polarization geometry is referred to as  $sf-fs$  hereinafter. With the central wavelength of the pump set at  $\lambda_p = 800$  nm, the central maximum of the phase-matching function  $\Phi(\omega', \omega_s, \omega_i)$  for this FWM process gives rise to an almost horizontal stripe at the center of the JSA map (Fig. 3a), representing  $\approx 98\%$  of the photon-pair generation probability. If only the entire signal bandwidth,  $\Delta\omega_s \approx 35$  THz, within this central lobe of the JSA map could be accommodated by a single spectral mode  $\psi_1(\omega)$ , the photon-pair output would be overwhelmingly dominated by biphotons with a factorizable wave function  $|\Psi\rangle$ .

Results of the Schmidt-mode analysis, presented in Fig. 3d, show that the structure of the central lobe in the JSA map in Fig. 3a can indeed be accurately approximated as a product of two spectral modes –  $\psi_1(\omega)$ , and  $\varphi_1(\omega)$ . This pair of modes enters into the Schmidt decomposition of Eq. (2) with a weighting factor  $\sqrt{\lambda_1} \approx 0.99$ , thus accounting for 99% of the two-photon state generated as the fiber output. The second largest  $\lambda_n$  coefficient in this expansion is almost two orders of magnitude smaller than  $\lambda_2$  (Fig. 3d). The purity of the photon-pair FWM output in this regime is  $p \approx 0.96$ . The entanglement entropy is  $S \approx 0.15$  (Fig. 2d). The effective dimensionality of the Hilbert space needed to describe the entanglement structure of such a two-photon state is  $K \approx 1.04$ .

It is pleasing that, with a rather simple fiber design, vectorial FWM can be steered toward high-purity photon-pair generation with a pump at around 800 nm – the central wavelength of Ti: sapphire short-pulse laser sources. Off this wavelength, the  $sf-fs$  FWM tends to deliver two-photon states whose continuous-variable spectral entanglement structure can only be described in a Hilbert space of higher dimensionality. Specifically, with the cross-polarized pump fields centered at  $\lambda_p = 850$  nm, the central lobe in the JSA map for this FWM process is tilted (Fig. 3b), indicating a positive correlation between different frequency components within broadband signal and idler FWM sidebands. In this case, the two-photon state  $|\Psi\rangle$  is no longer reducible to a single term in expansion (7), as several Schmidt-mode products in this expansion have nonnegligible  $\lambda_n$  (Fig. 3e), providing noticeable contributions to  $|\Psi\rangle$ . The two-photon state generated at the fiber output is thus no longer factorizable, but is given by a superposition of several pairs of Schmidt modes. The effective dimensionality of the Hilbert space needed to describe the entanglement of the photon-pair fiber output in this case is  $K \approx 3.4$ . The purity of the photon-pair FWM output is  $p \approx 0.29$ , with the entanglement entropy is  $S \approx 1.9$ .

An even larger number of Schmidt modes is needed to characterize the entanglement of the photon-pair output of an  $sf-fs$  FWM driven by cross-polarized pump fields centered at  $\lambda_p$

= 750 nm (Figs. 3c). In this case, the spectrum of  $\lambda_n$  extends to very high  $n$  (Fig. 3f), indicating that the two-photon state  $|\Psi\rangle$  is a superposition of a very large number of Schmidt-mode pairs. The effective dimensionality of the Hilbert space in this case is  $K > 400$ , correlation between different frequency components of the signal and idler fields is negative, the purity of the photon-pair output is as low as  $p \approx 0.002$ , and the entanglement entropy is at  $S \approx 6.5$ .

In Fig. 4, we present calculations performed for an  $sf-sf$  FWM process, in which two cross-polarized pump fields with the same central wavelength and identical Gaussian spectral profiles give rise to the signal and idler fields in the fast and slow modes, respectively (Fig. 1e). For this polarization geometry, two-photon states with the highest purity are achieved when the pump wavelength is set at  $\approx 670$  nm. The central lobe of the JSA map in this regime is vertical (Fig. 4a) and is accurately (with a  $\approx 1.5\%$  error) approximated as a product of  $\psi_1(\omega)$ , and  $\phi_1(\omega)$ . The two-photon state generated in this regime at the fiber output is dominated by the first term in expansion (7), with the largest Schmidt eigenvalue,  $\lambda_1$ , being  $\approx 60$  times larger than the second largest  $\lambda_n$  coefficient (Fig. 4d). The purity of this photon-pair FWM output is now  $p \approx 0.93$ , the effective dimensionality of the Hilbert space is  $K \approx 1.06$ , and the entanglement entropy is  $S \approx 0.26$  (Fig. 2f).

As the central wavelength of the cross-polarized pump is detuned off this wavelength, the central lobe in the JSA map becomes tilted (Figs. 4b, 4c), indicating positive (Fig. 4b) or negative (Fig. 4c) correlations between the frequency components of the signal and idler fields. With the pump wavelength set at  $\lambda_p = 700$  nm (Fig. 4c), an extended spectrum of  $\lambda_n$  (Fig. 4f) indicates a very high dimensionality of the Hilbert space,  $K > 70$ , needed to accommodate all the modes of the two-photon state produced at the fiber output. The purity of this state is as low as  $p \approx 0.01$ , while the entanglement entropy is  $S \approx 4.0$ .

Among other polarization FWM geometries, an  $ff-ss$  FWM process, in which both pump fields propagate in the fast mode, while the signal and idler fields are generated in the slow mode (Fig. 1b), stands out as an interesting setting enabling the generation of high-purity two-photon states. Indeed, with the pump wavelength tuned to  $\lambda_p = 800$  nm, this FWM process is seen to deliver two-photon states with a purity as high as  $p \approx 0.9$  (Fig. 2c), indicating a high factorizability degree of the photon-pair fiber output. The problem is, however, that, in this polarization geometry, FWM generates the signal and idler photons in the same polarization mode (Fig. 1b), thus lacking the elegance and power of FWM with cross-polarized pump ( $sf-fs$  and  $sf-sf$  polarization schemes in Figs. 1d and 1e), where the information-carrying modes can be easily addressed and manipulated using polarization optics.



#### IV. PULSE MODES AND CLASSICAL-FIELD DYNAMICS

While the spectral maps of the JSA function provide a powerful tool for visualizing the structure of quantum entanglement in the frequency domain, it is the time-domain Schmidt-mode analysis that offers, as we are going to show below in this section, a clear physical perspective of how exactly this entanglement structure builds up as a result of field-waveform dynamics and reveals a fundamental, correspondence-type relation between the quantum and classical pictures of photon-pair generation.

To gain these insights, we transform the Schmidt eigenfunctions  $\psi_n(\omega)$  and  $\varphi_n(\omega)$  into the time domain,

$$u_n(t) = \int \psi_n(\omega) \exp(-i\omega t) d\omega, \quad (11)$$

$$v_n(t) = \int \varphi_n(\omega) \exp(i\omega t) d\omega, \quad (12)$$

to represent the signal and idler field operators as expansions

$$\hat{E}_s(\eta, z) = \sum_n \hat{b}_n g_n(\eta), \quad (13)$$

$$\hat{E}_i(\eta, z) = \sum_n \hat{c}_n h_n(\eta), \quad (14)$$

where  $\eta_q = t - z/v_q$  is the time in the retarded frame of reference,  $t$  is the time in the laboratory frame of reference,  $z$  is the coordinate along the fiber,  $v_q$  is the group velocity, and  $q = p, s, i$  for the pump, signal and idler pulses. For the pump pulses,  $t = 0$  is chosen to correspond to the peak of the pulses at  $z = 0$ . Had these pulses remained undistorted in the course of pulse evolution in the fiber, their peaks would have stayed at  $\eta = 0$  at any  $z$ .

For high-purity two-photon states with JSA maps as those shown in Figs. 3a and 4a, with  $\lambda_1 \gg \lambda_n$  for any  $n > 1$ , expansion (2) for the JSA and expansion (7) for  $|\Psi\rangle$  are dominated by the  $n = 1$  term. A two-photon state with such a structure is composed, as Eqs. (13) and (14) show, of signal and idler pulse modes  $g_1(\eta)$  and  $h_1(\eta)$ . In Figs. 5a and 5b, we show these modes calculated as Fourier transforms of the eigenfunctions  $\psi_1(\omega)$  and  $\varphi_1(\omega)$  found by solving Eqs. (3) and (4) for two-photon states produced via  $sf-fs$  FWM with  $\lambda_p = 800$  nm and  $sf-sf$  FWM with  $\lambda_p = 670$  nm – FWM processes that deliver high-purity two-photon states (Figs. 2e, 2f). The two-photon state produced via  $sf-fs$  FWM with  $\lambda_p = 800$  nm (Fig. 5a) is seen to consist of a short signal pulse with a pulse width of  $\approx 300$  fs and a much longer idler pulse, which waveform is not immediately comprehensible. The structure of the photon pair in Fig. 5b is in many ways complementary, as the two-photon state in this case is a combination of a short idler pulse and a much longer signal pulse. The similarity in the

temporal structure of Schmidt-mode pairs of the two-photon states in Figs. 5a and 5b is striking.

To understand these results, we resort to the classical nonlinear dynamics behind the buildup of the signal and idler waveforms as a result of short-pulse FWM. Central to this analysis are effects related to the mismatch of the group velocities  $v_{p1}$ ,  $v_{p2}$ ,  $v_s$ , and  $v_i$  of the pump, signal, and idler pulses. In Figs. 5c and 5d, we present these group velocities calculated as functions of the wavelength for  $sf-fs$  FWM driven by 800-nm pump (Figs. 5c) and  $sf-sf$  FWM with a 670-nm pump (Figs. 5d).

For  $sf-fs$  FWM with  $\lambda_p = 800$  nm, the group velocity of the signal pulse is seen to fall in-between the group velocities of the pump fields propagating in the fast and slow modes of the fiber. The group velocity of the idler pulse, on the other hand, is considerably lower than the group velocities of the pump fields. With such a relation of the group velocities, the generation of the signal and idler fields is efficient only as long as the group delay between the pump fields is smaller than the pump pulse width. As  $v_s$  falls in the range right between  $v_{p1}$  and  $v_{p2}$ , such a nonlinear process gives rise to a short signal pulse whose pulse width corresponds to the bandwidth  $\Delta\omega_s$  of the central lobe in Fig. 3a. As long as they overlap in time, the pump and signal pulses continue to generate the idler field. However, since the group velocity of the idler pulse is appreciably lower than  $v_{p1}$ ,  $v_{p2}$ , and  $v_s$ , this pulse continuously lags behind the pump and signal pulses. As a result, the idler field waveform acquires a complicated temporal envelope with a sharp peak in its trailing edge, whose width is close to the signal pulse width and which is delayed relative to the signal pulse by a well-defined delay time.

With this classical picture in mind, we are tempted to estimate this delay time as  $\tau_d \approx L(v_i^{-1} - v_s^{-1})$ . This simple estimate gives  $\tau_d \approx 1.2$  ps (vertical dashed lines in Fig. 5a), which agrees remarkably well with the time separation between the temporal Schmidt mode of the signal field and the peak in the trailing edge of the pulse mode of the idler field.

For an  $sf-sf$  FWM process driven by a 670-nm pump (Figs. 1e), the relation of the signal and idler group velocities is in many ways opposite. Since it is now the group velocity of the idler pulse that falls in-between the group velocities of the pump fields polarized along the  $s$  and  $f$  fiber axes (Fig. 5d), the idler-wave output is a short pulse whose pulse width corresponds to the bandwidth  $\Delta\omega_i$  of the central lobe in Fig. 4a. Because the signal group velocity is now the lowest among all the pulses, it is now the signal pulse that continuously lags behind the other three pulses and acquires a complicated temporal envelope with a sharp peak in its trailing edge. The width of this peak is close to the idler pulse width. The time delay between the idler pulse and this peak in the trailing edge of the signal field waveform

agrees, once again, very closely with a simple estimate  $\tau_d \approx L(v_i^{-1} - v_s^{-1}) \approx 1.2$  ps, as shown by the vertical dashed lines in Fig. 5b.

Off the pump wavelengths providing suitable group-velocity relations, vectorial FWM generates two-photon states with a complex, high-dimensional structure of spectral entanglement, which can only be described in a Hilbert space of higher dimensionality. Specifically, for  $sf-fs$  FWM with a pump at  $\lambda_p = 750$  nm, both the signal and idler group velocities are considerably lower than the group velocities of both pump pulses (Fig. 5e). The two-photon state generated by such an FWM process is a broadband ket (1) whose entanglement structure is described in a high-dimensional space with  $K > 400$  (Figs. 3c, 3f). For  $sf-sf$  FWM with  $\lambda_p = 700$  nm, the signal and idler pulses are also seen to be substantially slower than the pump pulses (Fig. 5f), translating into a high-dimensional entanglement of the photon-pair FWM output with  $K > 70$  and purity as low as  $p \approx 0.01$  (Figs. 4c, 4f).

## V. CONCLUSION

To summarize, we have shown that vectorial four-wave mixing (FWM) of ultrashort laser pulses in a highly birefringent, highly nonlinear optical fiber can provide a source of broadband high-dimensional continuous-variable entanglement with finely tunable entropy and purity. We have demonstrated that the broadband photon-pair output of such a vectorial FWM can be steered, by varying the pump wavelength and polarization geometry, from a high-purity entangled ket to a high-entropy entangled state in a space of a very high dimensionality. The time-domain Schmidt-mode analysis has been shown to provide a clear physical perspective on how the entanglement structure of such two-photon states builds up as a result of short-pulse nonlinear dynamics. When viewed from this perspective, the pulse modes comprising high-purity two-photon states generated via vectorial FWM can be adequately understood in terms of classical-field short-pulse nonlinear dynamics. This insight reveals a correspondence-type relation between the quantum and classical pictures of photon-pair generation.

## ACKNOWLEDGMENTS

This research has been supported by the Government of Russian Federation (project no. 14.Z50.31.0040, Feb. 17, 2017).

## REFERENCES

1. Z. Xie, T. Zhong, S. Shrestha, X. Xu, J. Liang, Y.-X. Gong, J. C. Bienfang, A. Restelli, J. H. Shapiro, F. N. Wong, and C. W. Wong, *Nature Photonics* **9**, 536 (2015).
2. A. C. Dada, J. Leach, G.S. Buller, M.J. Padgett, and E. Andersson, *Nature Phys.* **7**, 677 (2011).
3. A. C. Dada, J. Leach, G. S. Buller, M. J. Padgett, and E. Andersson, *Nature Phys.* **7**, 677 (2011).
4. F. Steinlechner, S. Ecker, M. Fink, B. Liu, J. Bavaresco, M. Huber, T. Scheidl, and R. Ursin, *Nature Commun.* **8**, 15971 (2017).
5. M. Kues, C. Reimer, P. Roztock, L. R. Cortés, S. Sciara, B. Wetzel, Y. Zhang, A. Cino, S. T. Chu, B. E. Little, D. J. Moss, L. Caspani, J. Azaña, and R. Morandotti, *Nature* **546**, 622 (2017).
6. J. T. Barreiro, T. C. Wei, and P. G. Kwiat, *Nature Phys.* **4**, 282 (2008).
7. B. P. Lanyon, M. Barbieri, M. P. Almeida, T. Jennewein, T. C. Ralph, K. J. Resch, G.J. Pryde, J. L. O'Brien, A. Gilchrist, and A. G. White, *Nature Phys.* **5**, 134 (2009).
8. W.-B. Gao, C.-Y. Lu, X.-C. Yao, P. Xu, O. Gühne, A. Goebel, Y.-A. Chen, C.-Z. Peng, Z.-B. Chen and J.-W. Pan, *Nature Phys.* **6**, 331 (2010).
9. S. Lloyd, *Science* **321**, 1463 (2008).
10. Z. Zhang, M. Tengner, T. Zhong, F.N.C. Wong, and J.H. Shapiro, *Phys. Rev. Lett.* **111**, 010501 (2013).
11. M. Huber and M. Pawłowski, *Phys. Rev. A* **88**, 032309 (2013).
12. W. Tittel, J. Brendel, H. Zbinden, and N. Gisin, *Phys. Rev. Lett.* **81**, 3563 (1998).
13. R. T. Thew, A. Acin, H. Zbinden, and N. Gisin, *Phys. Rev. Lett.* **93**, 010503 (2004).
14. M. Krenn, M. Huber, R. Fickler, R. Lapkiewicz, S. Ramelow, and A. Zeilinger, *Proc. Natl. Acad. Sci. USA* **111**, 6243 (2014).
15. C. K. Law, I. A. Walmsley, and J. H. Eberly, *Phys. Rev. Lett.* **84**, 5304 (2000).
16. M. Erhard, R. Fickler, M. Krenn, and A. Zeilinger, *Light Sci. Appl.* **7**, 17146 (2018).
17. V. Ansari, J. M. Donohue, B. Brecht, and C. Silberhorn, *Optica* **5**, 534 (2018).
18. R. Fickler, R. Lapkiewicz, W. N. Plick, M. Krenn, C. Schaeff, S. Ramelow, A. Zeilinger, *Science* **338**, 640 (2012).
19. R. Fickler, R. Lapkiewicz, M. Huber, M. P.J. Lavery, M. J. Padgett, and A. Zeilinger, *Nature Commun.* **5**, 4502 (2014).
20. J. Leach, B. Jack, J. Romero, A.K. Jha, A.M. Yao, S. Franke-Arnold, D.G. Ireland, R.W. Boyd, S.M. Barnett, M.J. Padgett, *Science* **329**, 662 (2010).
21. A. Peruzzo, M. Lobino, J. C. F. Matthews, N. Matsuda, A. Politi, K. Poulios, X.-Q. Zhou, Y. Lahini, N. Ismail, K. Wörhoff, Y. Bromberg, Y. Silberberg, M.G. Thompson, J.L. O'Brien, *Science* **329**, 1500 (2010).
22. M.P. Edgar, D.S. Tasca, F. Izdebski, R.E. Warburton, J. Leach, M. Agnew, G.S. Buller, R.W. Boyd, and M.J. Padgett, *Nature Commun.* **3**, 984 (2012).
23. J. D. Franson, *Phys. Rev. Lett.* **62**, 2205 (1989).

24. L. K. Shalm, D. R. Hamel, Z. Yan, C. Simon, K. J. Resch, and T. Jennewein, *Nature Phys.* **9**, 19 (2013).
25. A. Cuevas, G. Carvacho, G. Saavedra, J. Cariñe, W.A.T. Nogueira, M. Figueroa, A. Cabello, P. Mataloni, G. Lima, and G.B. Xavier, *Nature Commun.* **4**, 2871 (2013).
26. J. E. Sharping, J. Chen, X. Li, P. Kumar, and R. S. Windeler, *Opt. Express* **12**, 3086 (2004).
27. J. G. Rarity, J. Fulconis, J. Duligall, W. J. Wadsworth, and P. S. J. Russell, *Opt. Express* **13**, 534 (2005).
28. K. Garay-Palmett, H. J. McGuinness, O. Cohen, J. S. Lundeen, R. Rangel-Rojo, A. B. U'Ren, M. G. Raymer, C. J. McKinstrie, S. Radic, and I. A. Walmsley, *Opt. Express* **15**, 14870 (2007).
29. J. Fulconis, O. Alibart, J. L. O'Brien, W. J. Wadsworth, and J. G. Rarity, *Phys. Rev. Lett.* **99**, 120501 (2007).
30. O. Cohen, J. S. Lundeen, B. J. Smith, G. Puentes, P. J. Mosley, and I. A. Walmsley, *Phys. Rev. Lett.* **102**, 123603 (2009).
31. P. D. Drummond, R. M. Shelby, S. R. Friberg, and Y. Yamamoto, *Nature* **365**, 307 (1993).
32. P. J. Mosley, J. S. Lundeen, B. J. Smith, P. Wasylczyk, A. B. U'Ren, C. Silberhorn, and I. A. Walmsley, *Phys. Rev. Lett.* **100**, 133601 (2008).
33. S. Parker, S. Bose, and M. B. Plenio, *Phys. Rev. A* **61**, 032305 (2000).
34. O. Roslyak, C.A. Marx, and S. Mukamel, *Phys. Rev. A* **79**, 033832 (2009).
35. M.G. Raymer, A.H. Marcus, J.R. Widom, and D.L.P. Vitullo, *J. Phys. Chem. B* **114**, 15559 (2013).
36. L. Upton, M. Harpham, O. Suzer, M. Richter, S. Mukamel, and T. Goodson III, *J. Phys. Chem. Lett.* **4**, 2046 (2013).
37. O. Takafumi, R. Okamoto, and S. Takeuchi, *Nature Commun.* **4**, 2426 (2013).
38. Y. Israel, S. Rosen, and Y. Silberberg, *Phys. Rev. Lett.* **112**, 103604 (2014).
39. P. Russell, *Science* **299**, 358 (2003).

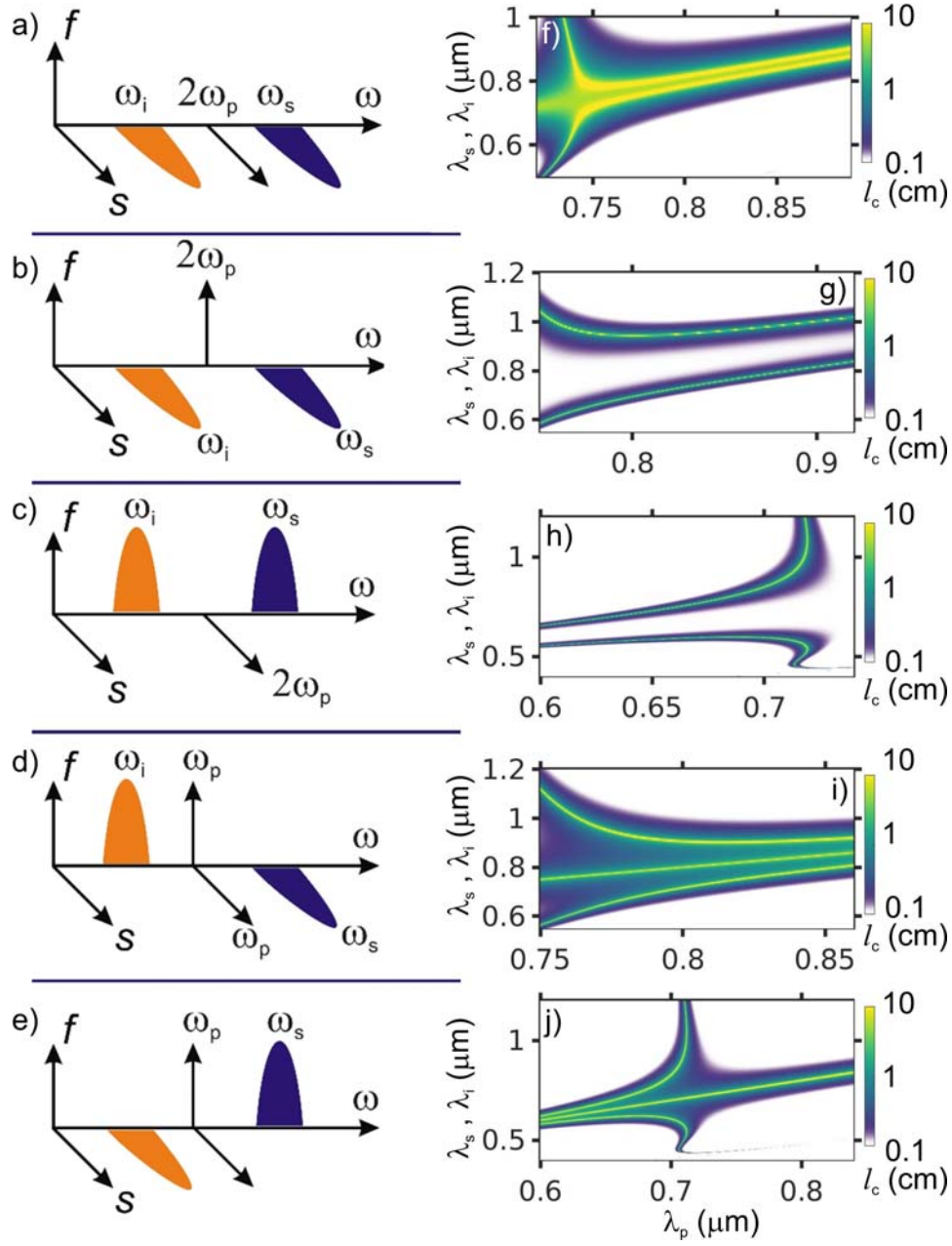


Fig. 1. (a – e) Polarization geometries in  $2\omega_p = \omega_s + \omega_i$  four-wave mixing in a birefringent optical fiber with fast and slow axes  $f$  and  $s$  and (f – j) the respective phase-matching maps, showing the coherence length  $l_c = \pi/|\Delta\beta|$  as a function of the pump, signal, and idler wavelengths for an optical fiber with  $\gamma = 100 \text{ W}^{-1} \text{ km}^{-1}$ ,  $\delta n = 10^{-4}$  (g, h),  $\delta n = 10^{-3}$  (i, j), and a GVD profile as shown in Fig. 2a: (a, f) scalar FWM, (b, g)  $ff-ss$ , (c, h)  $ss-ff$ , (d, i)  $sf-fs$ , (e, j)  $sf-sf$ .

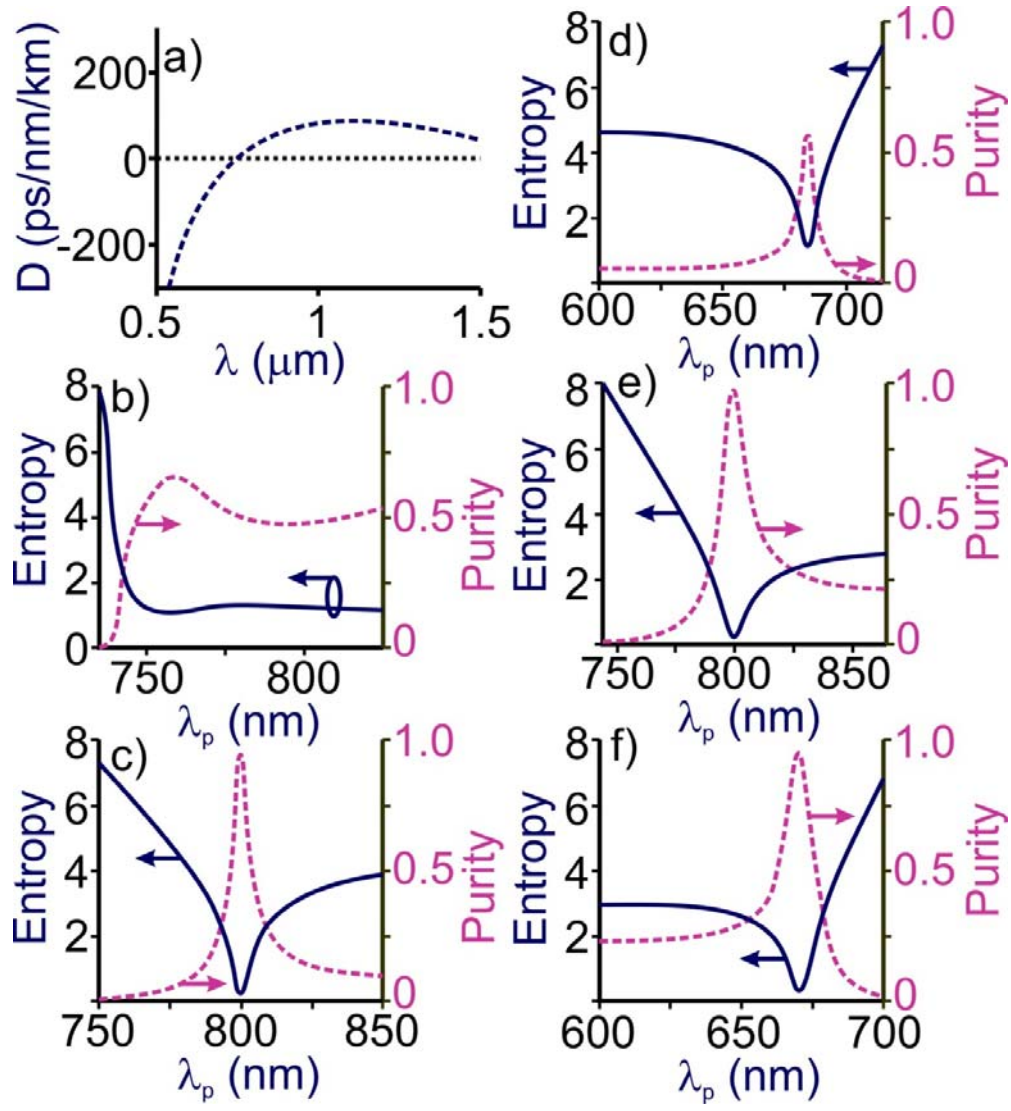


Fig. 2. (a) The group-velocity dispersion of the fiber used in calculations. (b – f) The entanglement entropy (blue solid line) and the purity of the two-photon states at the fiber output (pink dashed line) for different polarization geometries: (b) scalar FWM, (c)  $ff-ss$ , (d)  $ss-ff$ , (e)  $sf-fs$ , (f)  $sf-sf$ .

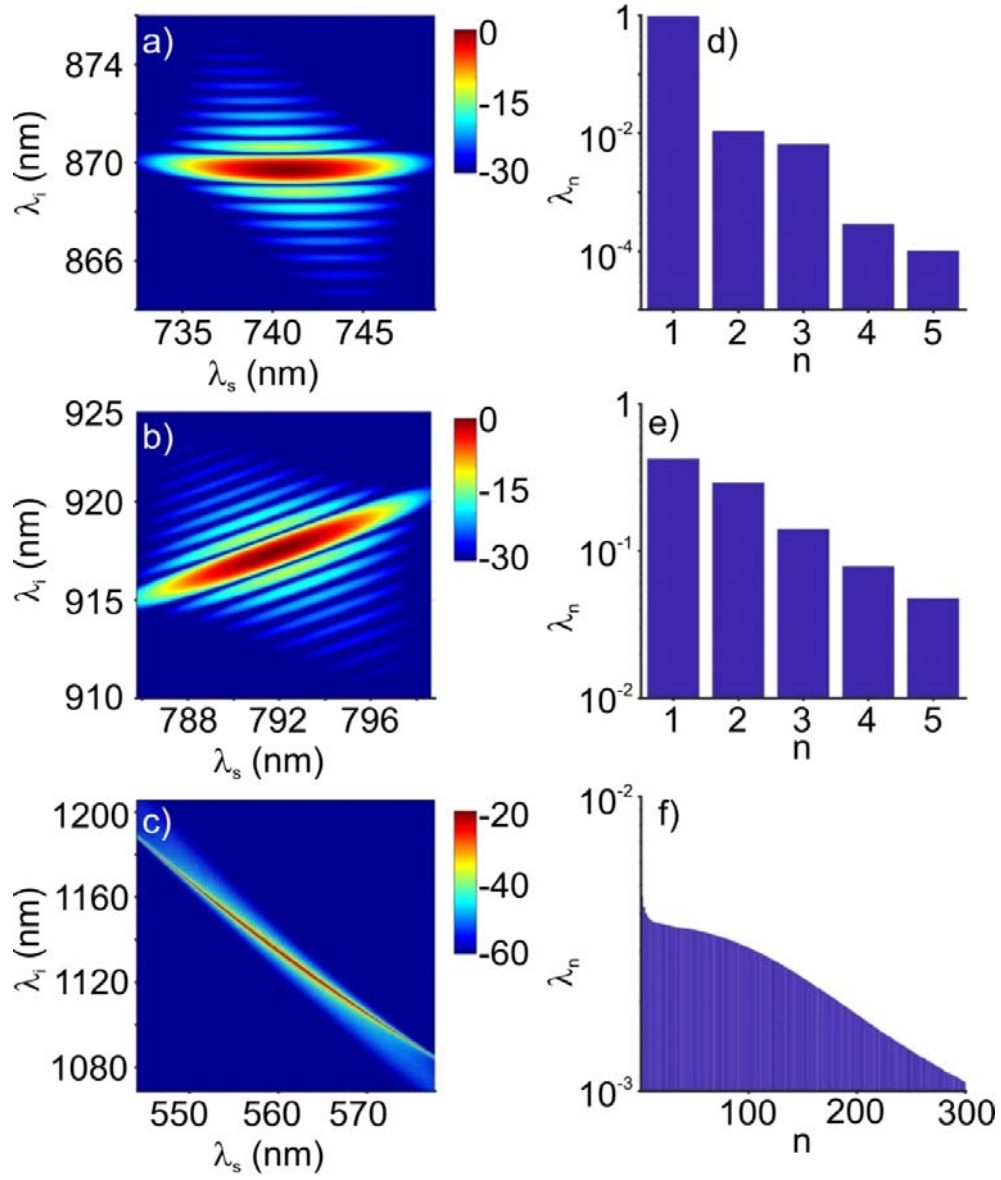


Fig. 3. (a – c) The joint spectral amplitude  $F(\lambda_s, \lambda_i)$  for the  $sf-fs$  polarization geometry of  $2\omega_p = \omega_s + \omega_i$  four-wave mixing. (d – f) The eigenvalues  $\lambda_n$  for a two-photon state generated through the  $sf-fs$  polarization geometry of  $2\omega_p = \omega_s + \omega_i$  four-wave mixing with a pump at  $\lambda_p = 800$  nm (a, d), 850 nm (b, e), and 750 nm (c, f).



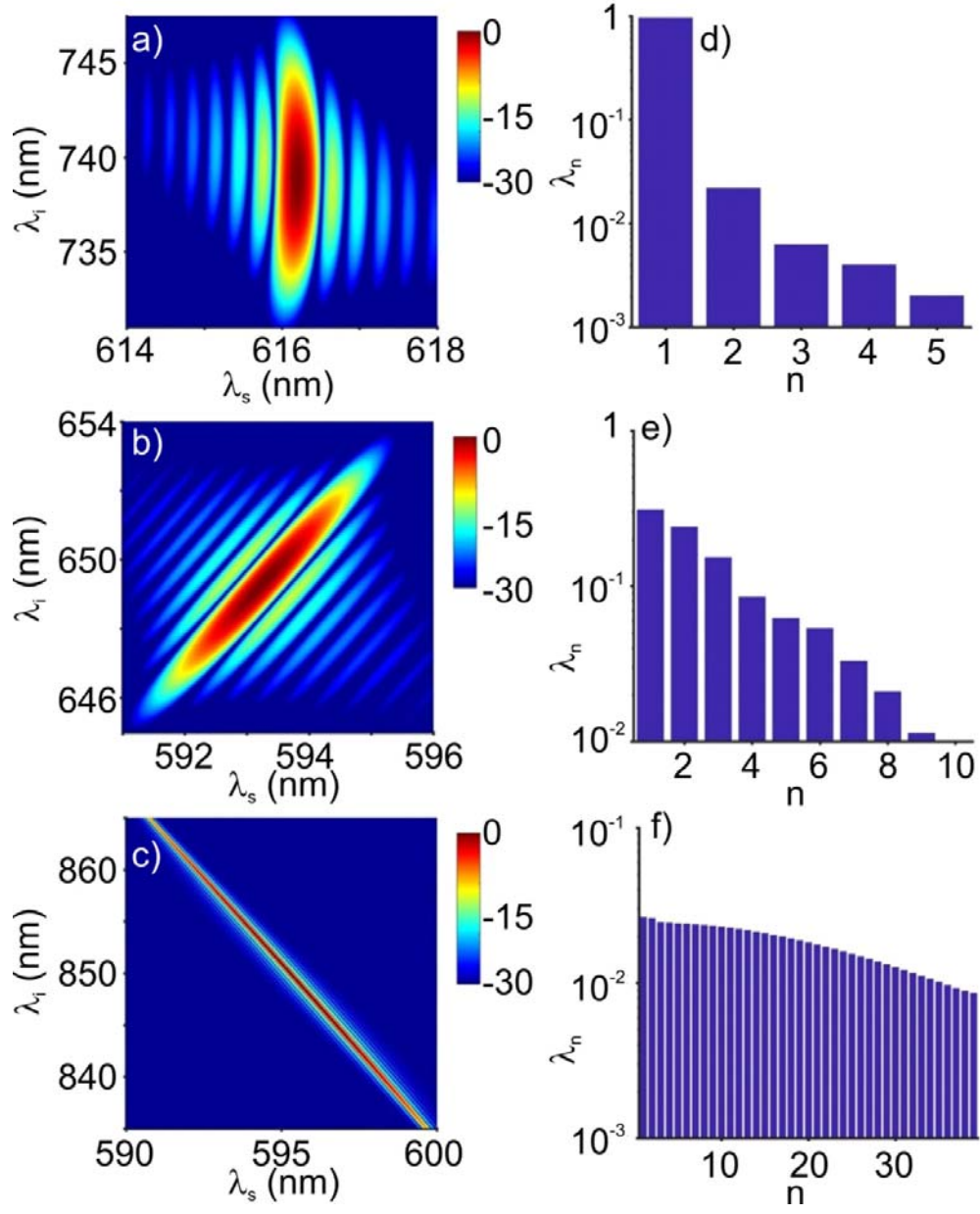


Fig. 4. (a – c) The joint spectral amplitude  $F(\lambda_s, \lambda_i)$  for the  $sf-sf$  polarization geometry of  $2\omega_p = \omega_s + \omega_i$  four-wave mixing. (d – f) The eigenvalues  $\lambda_n$  for a two-photon state generated through the  $sf-sf$  polarization geometry of  $2\omega_p = \omega_s + \omega_i$  four-wave mixing with a pump at  $\lambda_p = 670$  nm (a, b), 620 nm (b, e), and 700 nm (c, f).

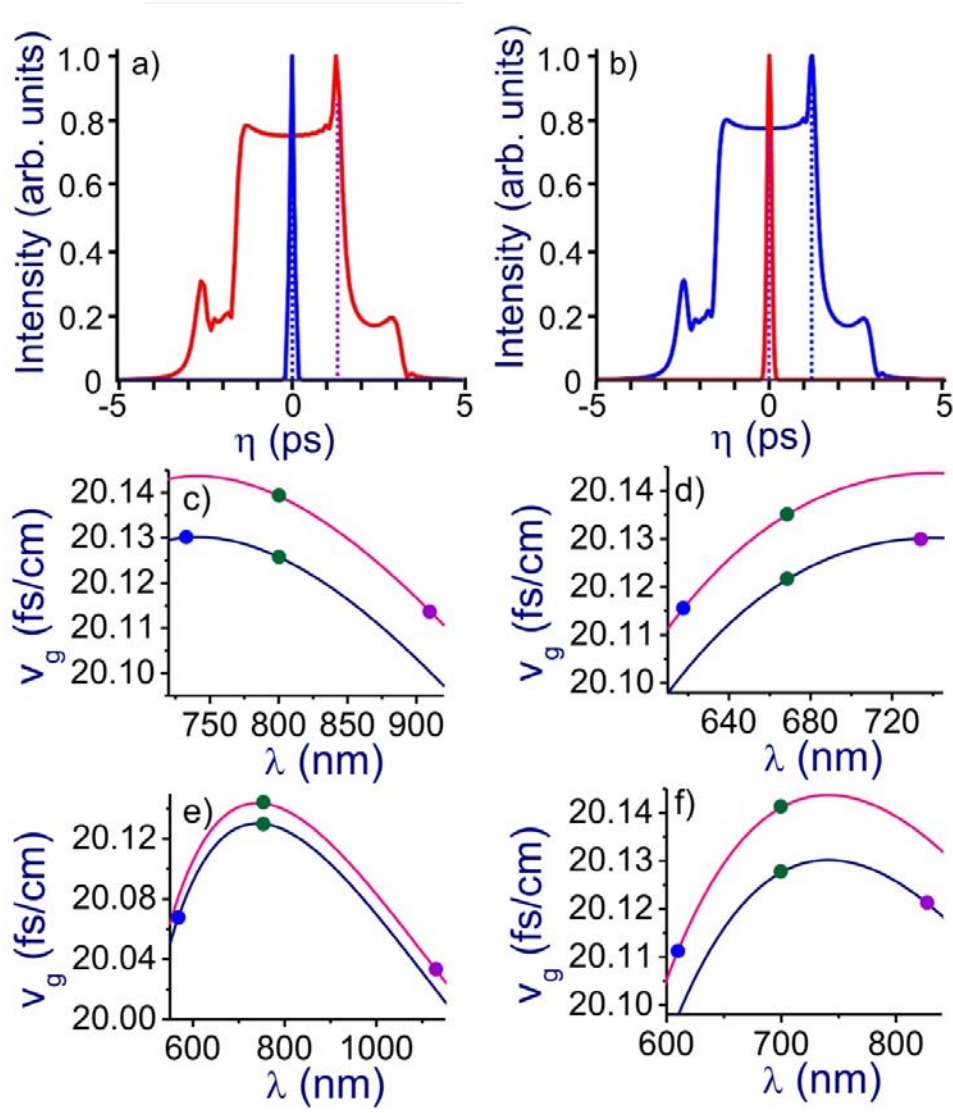


Fig. 5. (a, b) Signal (blue solid line) and idler (red dashed line) pulse modes produced as a part of the photon-pair fiber output and (d – e) the group velocities of the fast (pink dashed line) and slow (blue solid line) fiber modes as functions of the wavelength for  $sf - fs$  FWM with a pump at  $\lambda_p = 800$  nm (a, c) and  $750$  nm (e) and  $sf - sf$  FWM with  $\lambda_p = 670$  nm (b, d) and  $700$  nm (f). The group velocities of the signal, pump, and idler fields are shown by blue filled circles, green open circles, and purple squares.